Acta Biomaterialia xxx (xxxx) xxx

Contents lists available at ScienceDirect

Acta Biomaterialia

journal homepage: www.elsevier.com/locate/actbio

Full length article

Multimodal *ex vivo* methods reveal that Gd-rich corrosion byproducts remain at the implant site of biodegradable Mg-Gd screws

Niccolò Peruzzi[a,*], Silvia Galli[b], Heike Helmholz[c], Nikolay Kardjilov[d], Diana Krüger[c], Henning Markötter[e], Julian Moosmann[f], Dmytro Orlov[g], Zdenka Prgomet[h], Regine Willumeit-Römer[c], Ann Wennerberg[i], Martin Bech[a]

[a] *Medical Radiation Physics, Department of Clinical Sciences Lund, Lund University, Barngatan 4, 222 42 Lund, Sweden*
[b] *Department of Prosthodontics, Faculty of Odontology, University of Malmö, Carl Gustafs väg 34, 214 21 Malmö, Sweden*
[c] *Institute of Metallic Biomaterials, Helmholtz-Zentrum hereon GmbH, Max-Planck-Straße 1, 21502 Geesthacht, Germany*
[d] *Helmholtz Centre for Materials and Energy, Hahn-Meitner-Platz 1, 14109 Berlin, Germany*
[e] *Bundesanstalt für Materialforschung und-prüfung, Unter den Eichen 87, 12205 Berlin, Germany*
[f] *Institute of Materials Physics, Helmholtz-Zentrum hereon GmbH, Max-Planck-Straße 1, 21502 Geesthacht, Germany*
[g] *Materials Engineering, Department of Mechanical Engineering, LTH, Lund University, Ole Römers väg 1, 223 63 Lund, Sweden*
[h] *Department of Oral Biology and Pathology, Faculty of Odontology, University of Malmö, Carl Gustafs väg 34, 214 21 Malmö, Sweden*
[i] *Department of Prosthodontics, Institute of Odontology, University of Gothenburg, Göteborg, Sweden*

ARTICLE INFO

Article history:
Received 17 June 2021
Revised 22 September 2021
Accepted 26 September 2021
Available online xxx

Keywords:
Magnesium-gadolinium alloy
Biodegradable implant
Multimodal analysis
Energy-dispersive x-ray spectroscopy
Micro-computed tomography

ABSTRACT

Extensive research is being conducted on magnesium (Mg) alloys for bone implant manufacturing, due to their biocompatibility, biodegradability and mechanical properties. Gadolinium (Gd) is among the most promising alloying elements for property control in Mg alloy implants; however, its toxicity is controversial. Investigating Gd behavior during implant corrosion is thus of utmost importance. In this study, we analyzed the degradation byproducts at the implant site of biodegradable Mg-5Gd and Mg-10Gd implants after 12 weeks healing time, using a combination of different imaging techniques: histology, energy-dispersive x-ray spectroscopy (EDX), x-ray microcomputed tomography (μCT) and neutron μCT. The main finding has been that, at the healing time in exam, the corrosion appears to have involved only the Mg component, which has been substituted by calcium and phosphorus, while the Gd remains localized at the implant site. This was observed in 2D by means of EDX maps and extended to 3D with a novel application of neutron tomography. X-ray fluorescence analysis of the main excretory organs also did not reveal any measurable accumulation of Gd, further reinforcing the conclusion that very limited or no removal at all of Gd-alloy happened during degradation.

Statement of significance

Gadolinium is among the most promising alloying elements for property control in biodegradable magnesium alloy implants, but its toxicity is controversial and its behavior during corrosion needs to be investigated. We combine 2D energy dispersive x-ray spectroscopy and 3D neutron and x-ray tomography to image the degradation of magnesium-gadolinium implants after 12 weeks of healing time. We find that, at the time in exam, the corrosion has involved only the magnesium component, while the gadolinium remains localized at the implant site. X-ray fluorescence analysis of the main excretory organs also does not reveal any measurable accumulation of Gd, further reinforcing the conclusion that very limited or no removal at all of Gd-alloy has happened during degradation.

* Corresponding author.
E-mail addresses: niccolo.peruzzi@med.lu.se (N. Peruzzi), silvia.galli@mau.se (S. Galli), heike.helmholz@hereon.de (H. Helmholz), kardjilov@helmholtz-berlin.de (N. Kardjilov), diana.krueger@hereon.de (D. Krüger), henning.markoetter@bam.de (H. Markötter), julian.moosmann@hereon.de (J. Moosmann), dmytro.orlov@material.lth.se (D. Orlov), zdenka.prgomet@mau.se (Z. Prgomet), regine.willumeit@hereon.de (R. Willumeit-Römer), ann.wennerberg@odontologi.gu.se (A. Wennerberg), martin.bech@med.lu.se (M. Bech).

https://doi.org/10.1016/j.actbio.2021.09.047
1742-7061/

1. Introduction

Magnesium (Mg) and its alloys are increasingly appealing for bone implant manufacturing due to their biocompatibility, biodegradability and mechanical properties [1]. Mg-based materials have sufficient initial strength for the use in bone and degrade in the body into well-tolerated byproducts. This avoids the need of a second surgery for implant removal, which is especially desirable for patients. However, the challenge is to tailor the degradation such that it guarantees immediate fixation of the implants directly after the surgery, and a relatively fast degradation after healing is completed [2].

This can be controlled by adding alloying elements to pure Mg. Gadolinium (Gd) is particularly suitable as an alloying element, improving mechanical strength and corrosion resistance [3]. In addition, Gd is already used in medicine as a contrast agent for magnetic resonance. However, Gd toxicity is controversial [4] and investigating it is of utmost importance, before using it as implant material in the human body.

As a free ion, gadolinium ($Gd3+$) is extremely toxic [5,6] and has been shown to be an efficient calcium (Ca) antagonist [7]. In the case of implant biodegradation, it is generally assumed that the alloy will be rapidly and completely excreted from the body without release of Gd ions. However, a recent study has shown some accumulation of Gd in the organs (spleen, lungs, liver, and kidneys) after the placement of Mg-Gd pins in rats for 12 weeks [8]. Considering the similarity of $Gd3+$ to $Ca2+$, the maximum accumulation of Gd could actually be in the bone structure itself; such a phenomenon has been observed already in bone of human patients injected with Gd-based magnetic resonance contrast agents [9]. Another recent study [10], based on SAXS analysis of Mg-Gd implants, suggests instead that the Gd may remain incorporated in newly formed apatite at the implant site. These contrasting findings indicate the importance of investigating the elemental distribution of the corrosion byproducts in the proximity of the implant site.

Common elemental analysis techniques are x-ray fluorescence analysis (XRF) and energy-dispersive x-ray spectroscopy (EDX), which are both based on inducing emission of characteristic x-rays from the sample. Both techniques enable the quantification of elemental composition to investigate the spatial distribution of elements in life sciences. XRF has already been employed to show Mg accumulation in the proximity of Mg-based bioresorbable implants [11], as well as Gd deposition in the periodontal ligament of mice injected with Gd-based contrast agents [12]. Furthermore, the beneficial application of µ- and nano-XRF as non-destructive analytical tool has been demonstrated for biodegradable Mg- based implants in bone and an accumulation of constituents like yttrium has been shown [13,14]. Similarly, EDX is extensively used for corrosion studies of Mg-based implants [15] and EDX point analysis has already been employed to track multiorgan Gd deposition in a human patient with contrast-agent induced nephrogenic systemic fibrosis [16]. The present study has deployed EDX mapping in two dimensions (2D) to track the distribution of Mg and Gd in the corrosion layer and in the immediate proximity of Mg-Gd screws after 12 weeks of implantation in rat tibiae. Lab-based µXRF has also been used to measure Gd deposition in organs that had previously shown Gd accumulation in other studies [8].

While EDX and XRF can provide spatial information about the elemental composition of the samples at a very high resolution, they are typically regarded as surface techniques (EDX in particular, due to the shallow penetration of electrons). As such, they require slicing of the samples in order to access the interface of interest; furthermore, the information they provide is limited to a layer of depth equal to the penetration of the probe in the material. In order to access volumetric information and have a more complete picture of the corrosion behavior, we have applied x-ray and neutron micro-tomographic techniques.

Standard attenuation-based x-ray computed tomography in the micrometer-scale (µCT) is one of the most commonly used techniques to provide volumetric information but does not provide full elemental decomposition. Even though x-ray attenuation depends on the target material, this information alone is not enough to separate different elements, unless a-priori knowledge of the sample is postulated or more advanced techniques such as k-edge subtraction imaging (which nevertheless needs to be very selectively tuned for the materials of interest) are employed. An elemental discrimination can however be attempted by combining together different tomographic imaging modalities, as shown in recent studies that have merged x-ray and neutron tomography to separate between different elements [17,18]. Neutron tomography is particularly appealing for the investigation of Gd deposition, as Gd presents an extremely high attenuation coefficient for neutrons. As such, even a minor accumulation of Gd in the tissue surrounding the implant is expected to be clearly visible in a neutron tomography. In the present study, both synchrotron-based x-ray µCT and neutron µCT have been employed to assess the corrosion behavior in three dimensions (3D) of *ex vivo* Mg-Gd implants in bone.

The overall aim of the present work was to combine 2D EDX mapping and 3D neutron and x-ray tomography in order to investigate the degradation of Mg-Gd implants with different Gd concentrations (Mg-5Gd and Mg-10Gd, where 5 and 10 indicate the initial Gd weight percentage) after 12 weeks of healing time. A specific goal was to determine whether Gd remains incorporated within the corrosion layers at the implant site, diffuses into the bone near the implant site, or is excreted from the body without accumulation.

2. Materials and methods

2.1. Implants

Two different Mg alloys, with different Gd weight percentages (wt%), were used in this study: Mg-5Gd (5 wt%) and Mg-10Gd (10 wt%). The production procedure was well-characterized and described in detail in previous publications [19,20]. The alloys have also been characterized for their microstructure and degradation performance in a recent *in vitro* study [20]. The implants were 4 mm long, 2 mm diameter slotted grub screws, with an M2 thread. As reference material, titanium (commercially pure, grade 4) and polyether ether ketone (PEEK) screws, purchased from Promimic AB (Mölndal, Sweden), were also used. The Mg-Gd screws were gamma-sterilized, while the Ti and PEEK screws were cleaned in ultrasound baths and then autoclaved. Gamma-sterilization was preferred for the Mg-Gd screws as it has been proven to be one of the best sterilization methods to protect the material surface and to avoid unwanted and uncontrolled start of corrosion processes in Mg-based alloys, which might happen under the wet conditions of autoclaving [21].

2.2. Animal experiments

Ethical approval was received by the Malmö/Lund regional ethical board of the Swedish Board of Agriculture (number DNR M 188-15) to conduct this animal experiment. Within a broader project (SynchroLoad, Röntgen-Ångström Cluster project, number 05K16CGA), 108 Sprague Dawley adult male rats were operated. The rats were treated as described in previously published work [10]. In brief, after general narcosis and local anesthesia, the tibiae of the rats were exposed with a full-thickness flap and an osteotomy was created in each tibia. The rats received 1 screw in each hind leg and each rat received either 2 Mg-screws (Mg-10Gd

and Mg-5Gd screws, one in each leg) or 2 non-Mg screws (Ti and PEEK screws, one in each leg). The samples analyzed in the current study originated from 11 of the above-mentioned rats, euthanized after 12 weeks of healing, and were selected randomly to be allocated to the different tests.

2.3. Sample preparation

After euthanasia, the tibiae of the rats were harvested and bone-implant cylindrical blocks of 5 mm diameter were cut out with a trephine bur under irrigation. The blocks were fixed in 70% ethanol and then dehydrated in a series of ascending ethanol concentrations. Afterwards, the samples were critically point dried to be subjected to various test. For the current study, 11 samples were randomly selected, 4 Mg-10Gd, 4 Mg-5Gd and 3 Ti, all from the 12 weeks healing group.

All dried samples were scanned with high-resolution x-ray tomography. Two of them (1 Mg-10Gd and 1 Mg-5Gd) were subsequently kept dehydrated for neutron tomography scans. All the other blocks were instead rehydrated and embedded in methylmetacrylate by LLS Rowiak LaserLabSolutions GmbH (Hanover, Germany). Each embedded block was cut in half along the implant rotation axis with a 0.2 mm diamond band saw (Exakt Saw 300 CL, Exakt Technologies, Inc. OK, USA). The halves of 3 Mg-10Gd samples and 3 Mg-5Gd samples, as well as 3 Ti samples for control, were scanned with EDX without further preparation. After EDX, histological sectioning was also performed.

2.4. X-ray Tomography

X-ray tomography was carried out at the P05 Imaging Beamline (IBL) of the PETRA III storage ring at the Deutsches Elektronen-Synchrotron (DESY) in Hamburg, Germany, as previously published [19]. The x-rays were monochromatized with a double crystal monochromator to an energy of 34 keV. The tomograms were acquired by using a stepwise rotation with 1201 projections in total. The detecting system, which consisted of a scintillator coupled to a set of microscope optics and a CCD camera, provided a 7.39 mm horizontal field-of-view with 1.285 µm effective voxel size. Prior to reconstruction, the projections were 2 $\times$ 2 binned in order to improve the signal-to-noise ratio and make the file size more manageable for subsequent analysis. Dark- and flat-field correction, ring filtering and filtered back-projection were all performed with code developed in MATLAB environment [22], using the ASTRA toolbox [23–25]. A more extensive description of the x-ray tomographic setup and data acquisition is available in previously published work [19].

2.5. Neutron Tomography

Neutron tomography was performed with the high-resolution configuration at the V7 (CONRAD-2) instrument [26,27] of the BER-2 research reactor (Helmholtz-Zentrum Berlin). In addition to the two explants (1 Mg-5Gd and 1 Mg-10Gd, both 12 weeks healing time), a non-implanted screw of each alloy was also scanned for comparison. The polychromatic beam of cold neutrons was sent through a 3 cm pinhole, for a collimation ratio (L/D) of 167 on the measuring position (L = 500 cm). The samples were placed as close to the detector as possible (around 5 mm), in order to minimize image blur. Tomograms were acquired via stepwise rotation of the samples, covering the full 360° range with 600 projections in total. Each projection had an exposure time of 40 s, for a total scan time of approximately 13.5 h including overhead and additional flat and dark images (20 each). The detecting system [28], based on a 10 µm Gd_2O_2S scintillator optically coupled to a CCD camera with 2048 $\times$ 2048 pixels and 13.5 µm pixel size, was set to provide a 15.5 mm cropped field-of-view (the CCD was only partially illuminated) with 13 µm effective pixel size. The large field-of-view allowed to stack samples one on top of each other within the same scan, in order to optimize the beamtime. Dark and flat-field correction, ring filtering [29], beam-hardening filtering and filtered back-projection were performed with MuhRec [30].

2.6. Energy-dispersive x-ray spectroscopy

EDX mapping was carried out at the scanning electron microscope (SEM) E-SEM FEI Quanta 200 MKII system (Thermo Fisher Scientific) located at the Materials Engineering division of the Faculty of Engineering, LTH, in Lund. The machine was equipped with a Pegasus EBSD+EDX analytical system (EDAX, AMETEK), with an Octane Super SDD (60 mm^2 sensor) as EDX detector. Prior to being scanned, the samples were cleaned with an ultrasonic bath; they were then mounted on the SEM sample-holders with carbon tape. Conductive silver paint was used to form a conductive path from the sample-holder to the metallic implants. The scans were performed in high vacuum (1.56E-6 mbar), with a 15 V acceleration voltage, a 91 pA beam current and a 200 µs dwell time. Overview secondary-electrons SEM images were used to navigate the samples and to identify regions for performing EDX analysis. Depending on the size and position of accessible implant-bone interface, different amounts (between 3 and 6) and sizes of EDX maps were acquired on each sample. Data collection was performed on the TEAM™ software (EDAX, AMETEK).

2.7. Histology

After EDX analysis, the halves of the bone-implant blocks were subjected to histological preparation. The samples were polished to remove debris and then attached to plexiglasses for histological sectioning according to the cutting-grinding technique [31]. A 40 µm thick section was obtained from each sample and it was stained with Toluidine blue-Pironin y mixture to highlight bone and other tissues.

The slices were observed and photographed at a light microscope (Nikon Eclipse Ci-L equipped with DS-Fi3 camera and NiS D software, all Nikon, Tokyo, Japan).

2.8. X-ray fluorescence analysis of organs

The following organs were harvested *en toto* from 3 rats (2 with Mg-screws, 1 control), immediately after animal euthanasia: liver, spleen, kidneys, lungs, brain. The organs were immediately fixed in 70% ethanol for 1 week and were placed in 4% buffered formaldehyde until dehydration but not more than 1 month. Dehydration was carried out in ascending ethanol concentrations, followed by infiltration with isopropanol and finally embedding in paraffin. The embedded organ samples were sectioned with a microtome to expose a planar surface of more or less the center of the organs.

The paraffin blocks were analyzed by µXRF (Tornado M4 µXRF spectrophotometer; Bruker Nano, Berlin, Germany) for the determination of elemental composition in the selected soft tissues as described in [32]. In brief, a multipoint analysis was performed with an anode current of 200 mA. A grid of measurement points was generated automatically or manually depending on the size of the accessible tissue surface. Each measurement point constituted a technical replicate measurement of the tissue. The spectra were acquired for 30 s per point. An almost homogeneous sample coverage had to be achieved with a spot size of 25 mm. A background correction was enacted by measuring the plane paraffin surface without organic tissue. Data evaluation and image processing were performed with the Bruker ESPRIT microanalysis software version 1.3.0.3273.

2.9. Data analysis

The scans obtained with neutron tomography were registered to the matching x-ray µCT scans by means of semi-automatic data registration using the Amira Software (Thermo Fisher Scientific). Segmentation of the implants was then performed: in the neutron case, automatic grayscale thresholding in Amira was sufficient to separate the implants from the surrounding bone; in the x-ray scans, automatic segmentation of non-corroded implant, corrosion layer and bone was achieved with a machine learning approach [33]. Volume/surface renderings for data visualization were then created in Amira.

Semi-automatic registration was also performed to identify which slices in the x-ray µCT volumes corresponded to the EDX and histology planes. As a first step, histological pictures of the full samples were downscaled to a pixel size close to the one of the matching tomograms; they were also converted from RGB color into grayscale, by keeping only the brightness information and disregarding hue and saturation; lastly, they were "extended" from 2D pictures to 3D volumes by duplicating them once along the depth axis. This enabled the use of semi-automatic data registration tools in Amira, which would normally work either from 2D to 2D or from 3D to 3D. After registration, the x-ray µCT data were resliced in slices parallel to the histological plane. The slices that matched the EDX maps were then identified by visual inspection.

The EDX maps were energy calibrated with TEAM^{TM}; K-lines of relevant elements (or L-lines in the case of Gd) were then identified and used to produce intensity maps of only those selected elements. RGB maps were also created by combining the maps associated to three chosen elements at a time. In addition, the software provided standardless semi-quantitative concentrations of the different elements (in weight percentages, wt%) via ZAF corrections. Since the intensity of the Gd L-lines was deemed too low to perform such an analysis on an individual pixel basis, thresholding and manual selection tools were used to divide each map in three different regions of interest (ROIs), corresponding to non-corroded implant, corrosion layer and bone. In the controls, implanted with Ti screws, only a bone ROI was selected. In each ROI, the integrated spectrum was used to obtain semi-quantitative concentrations of the relevant elements, with associated uncertainty. Essentially, this corresponded to using each pixel of the EDX map as a replicate experimental measurement of the associated ROI, increasing the statistics at the cost of losing spatial resolution. Average concentrations in each class of ROIs and each implant alloy were then obtained by calculating the arithmetic mean of the values obtained from all the corresponding maps; the uncertainty associated to each value was selected as the maximum between the standard error of the values and the highest experimental uncertainty declared by the TEAM^{TM} software. A statistical comparison between the different groups was performed with one-way unbalanced ANOVA and post-hoc Tukey tests in MATLAB environment. A p-value below 0.05 was considered statistically significant.

3. Results and discussion

3.1. Overview

An example of the diverse information provided by the various imaging modalities that were employed in this work is presented in Fig. 1. In the histological picture (Fig. 1A), the toluidine blue has stained the biological tissue (bone and bone marrow) which surrounds the implant, but also seems to have penetrated in parts of the corrosion layer (arrows). The corrosion layer appears transparent to the illumination light, while the non-corroded metallic bulk of the implant is completely opaque. The corresponding x-ray µCT slice (Fig. 1B) provides more information about the implant: the corrosion layer appears to be divided in several "sub-layers", with varying x-ray attenuation. The non-corroded bulk presents a homogeneous attenuation, and its contours are in good agreement with the contours of the opaque region in the histology. The x-ray µCT slice that matches the plane of the EDX scans is presented in Fig. 1C, with superimposed RGB maps of which the red, green and blue channels correspond to the EDX maps of Gd, Ca and Mg respectively. The "sub-layered" structure of the corrosion-layer is well visible in the RGB EDX maps as a variation of Gd and Ca relative intensity (red and green), while the bulk appears to contain a homogeneous amount of Gd and Mg (red and blue). An in-depth analysis of a representative EDX map will be shown in the next sub-section (Section 3.2). Lastly, Fig. 1D shows a longitudinal slice of the implant in one of the neutron tomography scans. While the sample is not the same as in Fig. 1A–C, they are both Mg-5Gd 12w samples and its corresponding x-ray tomography (not shown) presented a layered-structure just like Fig. 1B. In the neutron case, the implant appears mostly homogeneous and highly attenuating, with no clear distinction between bulk and corrosion layer. The scan presents several artefacts due to beam starvation around the implant, and cupping-effects within the bulk of the implant, all stemming from the implant's high attenuation. The bone is completely overshadowed unless some overexposure is accepted in the implant, as in the picture. Highly attenuating particles are visible, detached from the implant (white arrow). A more detailed description and interpretation of the neutron results will be performed in Section 3.3.

3.2. EDX qualitative and semi-quantitative analysis

Multiple areas were scanned with EDX on each of the 6 samples (3 Mg-5Gd and 3 Mg-10Gd). In this section, the qualitative results of just one area of a Mg-5Gd sample (which is also identifiable in Fig. 1C) are presented; all the other scanned areas, independently on the alloy, showed very similar behavior and are provided without commentary as Supplemental Material together with their pixel size, which as mentioned in Section 2.9 gives an indication of the number of replicates available for the semi-quantitative analysis. The semi-quantitative analysis, described at the end of the section, encompasses all the areas for each alloy and reports the values for the controls (3 Ti) as well. No PEEK samples were scanned as controls, as their poor electrical conductivity would have caused electrical charging issues during the SEM acquisition; furthermore, since the focus of the study was evaluating the corrosion of Mg-Gd alloys and not the bone quality around the implants, Ti was considered sufficient as control material without any Mg-Gd presence.

From an analysis of the cumulative spectrum of the scans, six main elements of interest were identified: Mg, Gd, Ca, phosphorus (P), oxygen (O) and carbon (C). Fig. 2 shows the cumulative spectra corresponding to the three ROIs (non-corroded implant, outlined by blue dashed lines; corrosion layer, red solid outlines; bone, yellow dot-dashed outlines) in which the area was divided for the later semi-quantitative analysis. In the spectra, the emission lines of the aforementioned elements are labelled with black solid lines; smaller peaks could be reconducted to either pile-up and Compton edge peaks of the main elements (blacked dashed lines), or to trace elements (Na and K) which had a too low concentration to distinguish them from the background in the 2D maps and were thus discarded from the subsequent analysis.

The extracted 2D maps for each main element, normalized to their maximum intensity, are presented in Fig. 3, together with matching x-ray µCT and histology close-ups. Gd, Ca and Mg are presented in red, green and blue lookup tables respectively, in order to coincide with the RGB picture; the other three elements are shown in a grayscale lookup table.

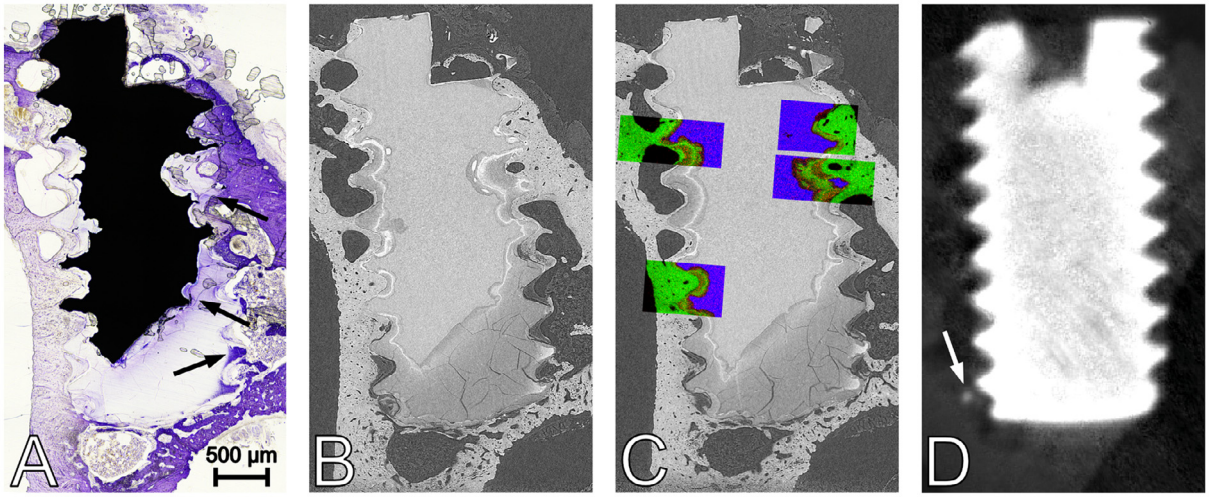

Fig. 1. Overview of the information provided by the different techniques employed in this work. A–Histological section of a Mg-5Gd sample. The staining agent (Toluidine blue-Pironin y mixture) has stained the biological tissue, but also seems to have penetrated in parts of the corrosion layer (arrows). The scalebar, 500 µm, applies to all the figures in this group. **B**–X-ray µCT slice which corresponds to the histological slice shown in A. **C**–X-ray µCT slice that matches the plane of the EDX scans (approximately 85 µm away from the slice shown in B), with superimposed RGB maps in which the red, green and blue channels correspond to the EDX maps of Gd, Ca and Mg respectively. **D**–Longitudinal slice of a Mg-5Gd sample in a neutron tomography scan. Highly attenuating particles are visible, detached from the implant (white arrow).

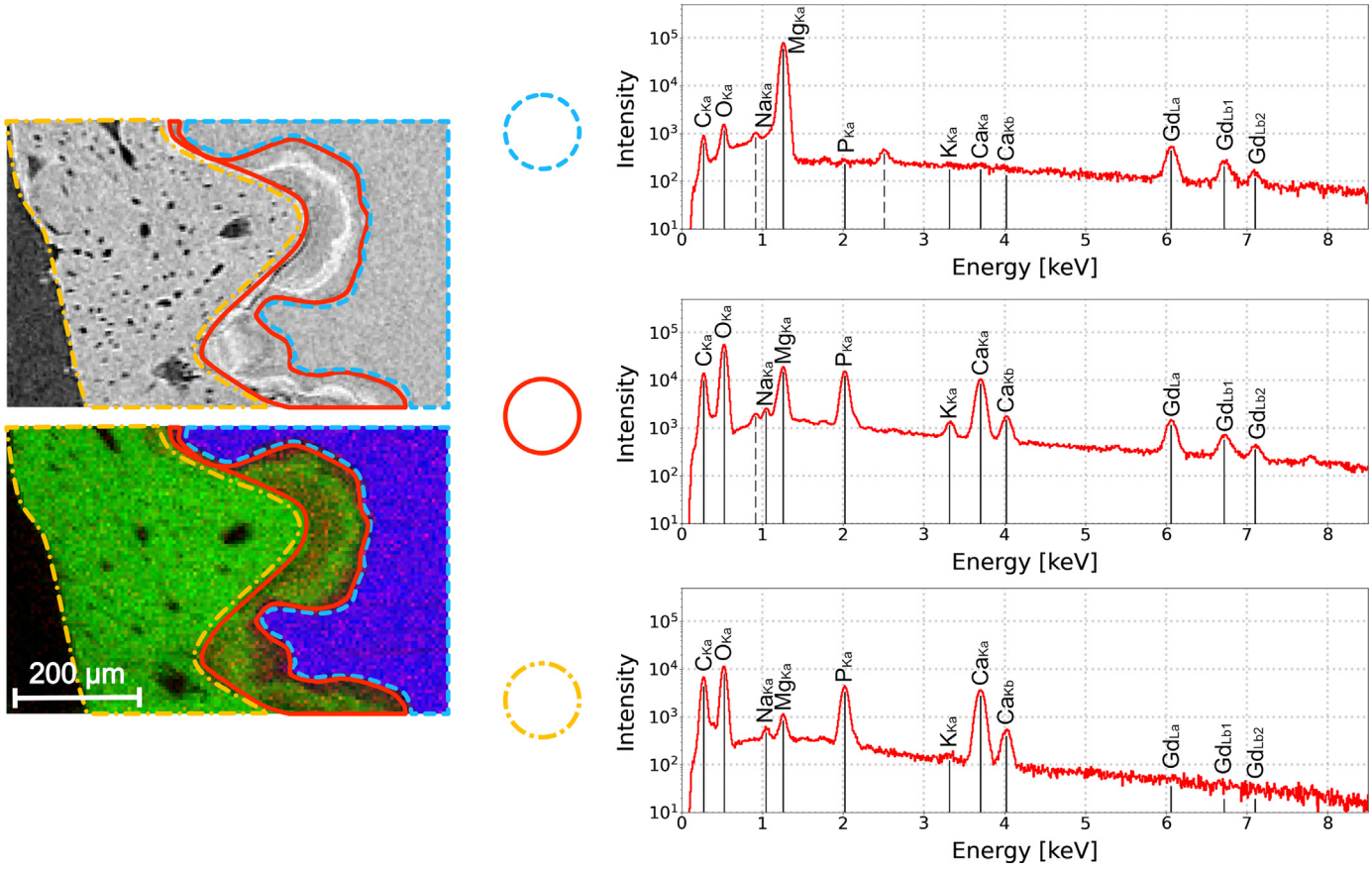

Fig. 2. Example of ROI selection and cumulative spectra in a representative EDX scan. The selected area, identifiable also in Fig. 1C, is shown both in the x-ray µCT domain (top image, in grayscale) and as an EDX RGB map with Gd, Ca and Mg channels respectively. The scalebar, 200 µm, applies to both figures. Three different ROIs are outlined on the images, and their cumulative EDX spectrum is shown on the right. Blue dashed outlines, top spectrum: non-corroded implant ROI. Red solid outlines, middle spectrum: corrosion layer ROI. Yellow dot-dashed outlines, bottom spectrum: bone ROI. In each cumulative spectrum, the emission lines of the main elements found in the samples are labelled with black solid lines. Black dashed lines are used for peaks not associated to real elements but caused by detection artefacts (pile-up peak and Compton edge, both from the Mg peak).

The Gd signal appears constant across the whole implant, without any visible distinction between non-corroded part and corrosion layer. A lower intensity signal would seem visible in the bone region as well, but a comparison with the corresponding spectrum in Fig. 2 indicates that the signal is most probably due to a constant background rather than real presence of the element. It was decided not to remove the background on the 2D maps, since the number of counts for the L-lines of Gd was prohibitively low on a pixel-by-pixel basis and a background fitting algorithm would risk removing real peaks as well. The fact that Gd still follows the original shape of the implant and does not seem to have been eroded away is consistent with what has been observed for other rare-earth (RE) metals (La and Ce) in an *ex vivo* study on rabbits with very long healing times [34]. Furthermore, it agrees with the hypothesis of it remaining incorporated in newly formed apatite at the implant site, described in the introduction [10].

The Mg map shows a homogeneous concentration in the non-corroded part of the implant, with a sharp decrease to much lower values in the corrosion layer. The contours are in good agreement with the homogeneous x-ray attenuation part of the x-ray µCT scan, and with the opaque metallic part of the histological scan.

As for Ca, its distribution shows a homogeneous concentration within the bone in the proximity of the implant, and a diffusion within the corrosion layer. The diffusion presents a concentration gradient, with the highest Ca concentration distributed in a layer which follows the contours of the non-corroded high-Mg part, as clearly visible in the RGB map. The high Ca layer matches very well the high x-ray attenuation layer in the x-ray µCT scan. In this particular example, it appears to be visible in the histology as well, as a thin line with hue similar to the color of non-stained bone; a high magnification analysis of the histological section, however, did not reveal the presence of any visible cells in it (Fig. 3).

Regarding the other elements: C is mostly associated with the resin embedding of the samples, with a high concentration in the bone lacunae and in the embedding material itself; O appears uniformly distributed all across the sample, with higher accumulation in the corrosion layer closest to the high-Mg ROI; P appears to closely match Ca but penetrates deeper in the corrosion layer. This latter behavior can be highlighted with an RGB image with P, Ca and Mg channels respectively (Fig. 4). The yellow color corresponds to co-presence of P and Ca, while the red layer immediately adjacent to the blue area indicates an accumulation of P next to Mg, with no Ca presence.

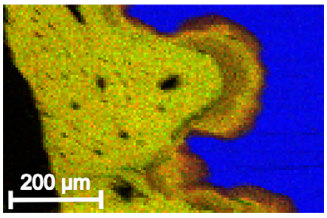

Fig. 4. EDX RGB image of P-Ca-Mg. RGB map of the same representative area as in Fig. 3. The red, green and blue channels are the EDX maps of P, Ca and Mg respectively.

The layered structure of the corrosion layer, with sub-layers rich in Ca, P and O, is consistent with what is known in literature about the formation of precipitates as a protective layer. In particular, a highly x-ray attenuating and Ca-rich sublayer has been observed during *in situ* corrosion of Mg-2Ag [35] and *in vitro* degradation of pure Mg [36]. Previous *in vitro* studies of Mg-10Gd alloys [37,38] had shown co-presence of Ca and P, but no sub-layered structure; their observation times however were much shorter than ours and their alloy presented a faster degradation rate. The degradation rate in particular has been suggested to be linked to the formation of such a Ca-rich sublayer [36]. These observations, coupled with the lack of any visible cells in the matching area of the histological section, indicate that, at least in the presented map, the accumulation of Ca and P is mostly linked to the corrosion processes of Mg, rather than bone-remodeling within the corrosion layer. A similar pattern was observed in the other areas of this sample, and in most of other samples. In some cases, a direct comparison with histology was not possible since the histological slice was quite different from the EDX plane, due to mechanical erosion of the sample during preparation for the histology.

The semi-quantitative results obtained from all the EDX analysis are presented in Table 1. While the reduction in Mg relative concentration between non-corroded parts, corrosion layer and bone was confirmed as statistically significant, the difference in Gd wt% between non-corroded and corroded was not (p-value = 0.85 for Mg-5Gd, p-value = 0.49 in the case of Mg-10Gd). A significant variation in Ca and P was also observed between corrosion layer

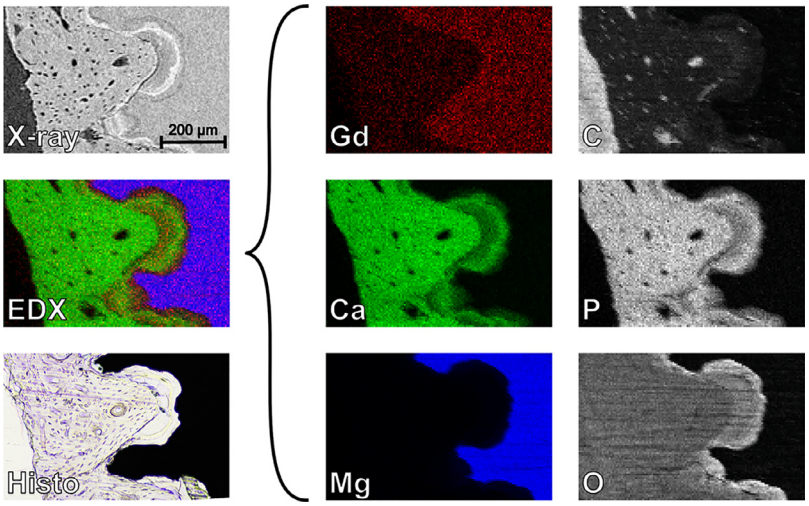

Fig. 3. Close-up comparison between EDX, x-ray µCT and histology. The same area as in Fig. 2 is shown as x-ray µCT (top-left), EDX Gd-Ca-Mg RGB map (middle-left) and histology (bottom-left). The EDX map is further separated in 2D maps for each main element, normalized to their maximum intensity: Gd, Ca and Mg are presented in red, green and blue lookup tables respectively, in order to coincide with the RGB picture; C, P and O are shown in a grayscale lookup table. The scalebar, 200 µm, applies to all the figures.

Table 1
Results of EDX semi-quantitative analysis. The relative concentration (in weight %) of the main elements of interest is presented, with associated standard error, for the different sample types and different ROIs. Where no result is reported the quantities were below the detection limits of the instrument. Superscripts indicate statistically significant variations when non-corroded and corrosion layer ROIs (letter a), corrosion layer and bone ROIs (letter b) and control bone and test bone ROIs (letter c) were compared.

ROI type	Mg	Gd	Ca	P	O	C
Mg-10Gd						
non-corroded	72 ± 3 [a]	8.8 ± 0.3	/	/	8.5 ± 1.6 [a]	7.9 ± 1.6 [a]
corrosion layer	14.3 ± 1.8 [a,b]	9.4 ± 0.5	9.0 ± 1.0 [b]	7.9 ± 0.9 [b]	42 ± 4 [a]	17 ± 2 [a]
bone	1.8 ± 0.2 [b]	/	24.6 ± 1.5 [b,c]	11.8 ± 0.5 [b,c]	46 ± 5	15 ± 3
Mg-5Gd						
non-corroded	80.7 ± 0.9 [a]	3.97 ± 0.11	/	/	4.6 ± 0.9 [a]	10.6 ± 1.4
corrosion layer	10.5 ± 1.1 [a,b]	4.4 ± 0.3	12.2 ± 1.1 [b]	8.2 ± 0.6 [b]	49 ± 4 [a]	14.7 ± 1.8
bone	1.3 ± 0.2 [b]	/	24.7 ± 0.9 [b,c]	11.8 ± 0.4 [b,c]	48 ± 5	13.3 ± 1.5
Ti						
control bone	0.49 ± 0.3	/	35.3 ± 1.3 [c]	14.9 ± 0.5 [c]	44 ± 4	12.0 ± 1.1

and bone ROIs; this is consistent with previous *in vitro* studies of Mg-10Gd corrosion [38], and further suggests that Ca and P accumulation in the corrosion layer is linked to Mg degradation rather than bone remodeling. Lastly, O presented a significant wt% reduction in the non-corroded material compared to the other two ROIs, but no significant difference between bone and corrosion layer. C did not show statistically significant differences between the various ROIs and alloys, with the exception of the non-corroded part of the Mg-10Gd samples, which presented a lower wt%; the fact that C is mostly associated to the resin in which the samples were embedded, however, leads to the belief that this could be a systematic error exacerbated by the low number of samples. When the two different alloys were compared between them, no significant difference was observed for any concentration, with the exception of Mg and Gd in the implant areas, proportional to the nominal alloy compositions (as expected). The table also reports the values obtained in the EDX analysis of control bone, i.e. the one in the proximity of Ti implants. Both Ca and P wt% were significantly higher in the controls than in the Mg-Gd samples, suggesting a difference in mineralization induced by the presence of the Mg-Gd implants. Since a study of bone quality was beyond the scope of this study, no further attention was given to this aspect. A more accurate study of this phenomenon would require more samples and additional time-points; furthermore, additional methods would be needed to better assess bone quality. The difference in Mg wt% was found to be not statistically significant, which indicates that, despite the high amount of Mg leaving the implants, the organism was quite efficient in removing any excess. This appear consistent with the observations by Grunewald et al. [11], who revealed an only transient accumulation of Mg, focused around bone vessels.

3.3. Neutron tomography

In the neutron scans, the implants appeared extremely attenuating and mostly homogeneous, as already anticipated in Fig. 1D. This was in stark contrast with the matching x-ray scans, in which the implants presented corrosion layers very similar to the ones already shown for the samples scanned with EDX. An example of this is given in Fig. 5, where a longitudinal section of the Mg-10Gd implant in the neutron domain (5A) is directly compared to its matching section in the x-ray domain (5B). Given that the neutron attenuation coefficient of Gd is orders of magnitude higher than the one of all the other elements expected in the sample [39,40], it seems reasonable to assume that the strong attenuation observed in the neutron scans is mostly due to the presence of Gd. While the implant in Fig. 5A shows higher attenuation on the edges compared to its center, this effect is most probably due to an insufficient correction of the cupping effect caused by the high attenuation and the wide neutron spectrum leading to beam hardening. In fact, both cupping and streak artefacts are much stronger in Fig. 5A than in Fig. 1D (which was a slice of the Mg-5Gd sample), because of the higher concentration of Gd and hence stronger attenuation. Furthermore, similar artefacts were observed for the non-implanted screws (shown as Supplemental Material), which were expected to be completely homogeneous, again supporting the case that the observed variations are linked to reconstruction artefacts.

The fact that the implant appears intact in the neutron domain, with no visible distinction between non-corroded and corroded parts, is consistent with the fact that Gd remains incorporated at the implant site, as directly observed with EDX. The advantage of neutron tomography over EDX is providing this information in a volumetric way, confirming that the behavior is consistent across the whole sample, rather than just in a fortunate 2D slice. The 3D aspect of the result is highlighted in Fig 5C–F: the neutron scans allow to separate the implant from the bone (5C) and confirm that the screw appears mostly intact in the neutron domain, i.e. as far as Gd is concerned (5D). This is not what one would have expected from x-ray tomography, in which the corrosion of the implant appears quite diffuse (5E) and the non-corroded part (5F) is very different from the original implant shape. An analysis of the corrosion dynamics of the implants, using x-ray µCT scans of all the samples and time-points described in the sample preparation section, in order to evaluate parameters such as degradation rate, bone volume over total volume and bone-to-implant-contact, is the topic of a different work (in submission).

The only change in shape from a neutron point of view is given by the detachment of small implant particles, which coincide with fractures of the corrosion layer in the x-ray domain (arrow in Fig 5A and B). These small particles were observed for both alloys and could be found at various distances from the intact implant (arrow in Fig. 1D). Since the debris was found in the bone marrow close to the implant, it is unclear whether the detachment might have happened during the corrosion or because of the mechanical preparation of the samples, following the harvesting. Even if real, this fragmentation is much slower than what had been observed in the study from Myrissa et al., in which Mg-10Gd pins had completely disintegrated in small particles after 12 weeks of implantation [8]. The discrepancy is most probably due to differences in material casting and in implant shape and had not been anticipated when planning the study. Extending our study to even longer time points could provide further insights on the disintegration mechanisms of the implants, in particular whether the Gd remains in place indefinitely (similar to other RE metals observed at the implant site 9 months after implantation [34]) or if the degra-

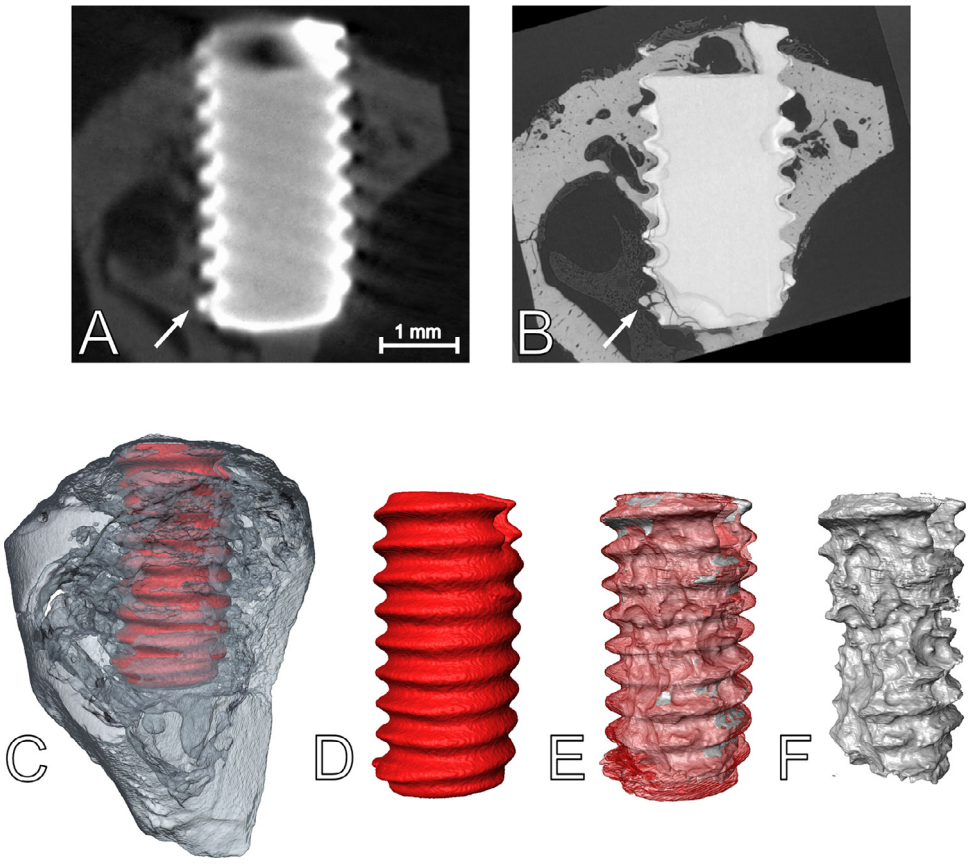

Fig. 5. Comparison between neutron and x-ray tomography. A longitudinal section of the Mg-10Gd implant in the neutron domain (**A**) is directly compared to its matching section in the x-ray domain (**B**). Detachment of parts of the corrosion layer is visible with both methods (white arrow). The scale bar, 1 mm, applies to both the figures. **C-F**: 3D renderings obtained from the volumetric scans. In the neutron scan, the implant, in red, can be separated from the bone, in transparent gray (**C**), and confirmed to appear mostly intact (**D**). In the x-ray scan, the corrosion layer, in transparent red, appears quite diffuse (**E**) and the non-corroded part, in solid gray, is very different from the original implant shape (**F**).

Table 2
Element composition (mass%) in soft tissue preparations measured by μXRF. Traces of Mg and Cu were detected but not evaluated, Gd was not detectable, mean (SD), n = number of data points per organ, control–1 animal; Gd–implantation Mg-5Gd and Mg-10Gd screw per leg for 12 weeks–two animals averaged.

organ	treatment	P	S	K	Ca	Fe	Zn	n
liver	control	20.90 (2.80)	42.94 (4.15)	14.37 (2.82)	4.23 (1.19)	7.33 (2.46)	1.74 (0.50)	232
	Mg-10Gd	20.83 (4.50)	41.86 (4.66)	15.25 (3.22)	4.71 (1.41)	10.14 (2.44)	1.70 (0.55)	261
lung	control	22.28 (4.92)	35.83 (6.66)	17.87 (4.90)	5.99 (1.87)	8.35 (3.79)	0.90 (0.44)	164
	Mg-10Gd	18.24 (4.73)	35.38 (4.54)	18.00 (3.34)	5.79 (1.39)	17.12 (6.29)	1.01 (0.42)	253
kidney	control	16.26 (3.75)	50.62 (7.59)	13.18 (2.29)	5.33 (1.34)	7.11 (2.78)	1.21 (0.78)	137
	Mg-10Gd	19.10 (3.04)	41.74 (4.40)	17.57 (3.15)	6.43 (1.66)	8.81 (2.09)	1.47 (0.467)	159
spleen	control	17.89 (3.11)	22.01 (5.96)	7.73 (1.50)	1.91 (0.49)	43.86 (8.78)	0.85 (0.27)	46
	Mg-10Gd	14.34 (4.66)	14.77 (4.25)	5.46 (1.52)	1.96 (0.61)	59.22 (11.53)	0.85 (0.22)	155
brain	control	23.35 (2.95)	46.45 (3.82)	16.17 (2.45)	8.36 (2.19)	1.47 (0.56)	1.15 (0.39)	55
	Mg-10Gd	24.48 (3.30)	40.20 (5.37)	18.69 (5.14)	8.23 (2.19)	1.79 (0.89)	1.11 (0.40)	171

dation in small particles will eventually result in a complete removal of the Gd. As our measurements have shown, any remaining small detached particles would still be easily distinguishable with neutron imaging, as long as they contain Gd.

3.4. Element analysis in soft tissue preparation

The results of the XRF analysis of the organs are presented in Table 2 as mass percentage (mass%). The number of measurement points per organ, which corresponds to the number of replicate experimental measurements, is given in the last column. The values show typical organ distributions, with a high Fe (hemoglobin) content in spleen and a higher S (protein) amount in liver, kidney and brain. Due to the low sensitivity of the instrument for Mg, the detected traces were not evaluated quantitatively. No Gd could be quantitatively measured in the selected organs of the exposed animal. An additional area scan of the brain of a Gd treated animal revealed no local enrichment of this element. Elements with an atomic number above 40 can be detected in the range of 10–100 ppm [41].

This is once again in very good agreement with our findings, confirming the hypothesis that Gd is not being removed from the implant site at the healing time in exam.

In addition to the focus on the implant components, remarkable differences have been detected for potassium, sulfur and iron. In particular, the potassium level was elevated in the liver, lung

and kidney of the treated animal. While these findings were interesting under a physiological aspect and verify element distribution results in other *in vitro* studies [32,42], detailed investigation on this issue has not been performed in the present study.

3.5. Limitations and future directions

While this work analyzed the elemental composition of the degradation byproducts with a fair variety of techniques, which furthermore all point to the same conclusion regarding Gd permanence at the implant site, there are nevertheless a few limitations that would need to be addressed in eventual follow up studies.

The first obvious limitation of this study is that it has only focused on one time point. Since our conclusion is that after 12 w of healing time Gd is still mainly localized at the implant site, it remains unclear how this behavior could affect the potential toxicity of the implants in the long term. Further studies with longer time points will be necessary in order to determine whether the implant eventually fully disintegrates and is flushed from the body, or if it stays in place indefinitely, potentially releasing toxic ($Gd3+$) ions in the surrounding bone over time. In this direction, it might also be beneficial to perform minimally invasive tests such as blood analyses on the animals at regular intervals, in order to look for Gd traces or increased Mg concentration during implant corrosion.

Another possible shortcoming of this study lies in the XRF results, which have only provided negative results regarding Gd presence in any of the major excretory organs. While XRF has been used in order to preserve the samples for future studies, more sensitive but destructive techniques could have been able to reveal very low concentrations of Gd in the organs that XRF might have missed. In particular, inductively coupled plasma mass spectrometry (ICP-MS) and inductively coupled plasma atomic emission spectroscopy (ICP-AES) have already been used to track Gd presence in soft tissue with very high sensitivity [8,43], and would be recommended if sample preservation is not of concern. Another possibility, albeit quite remote, is that small alloy particles might have been excreted without any residuals in the excretory organs. In this study we did not keep track of eventual Mg-Gd alloy presence in the animals' litter, which could have provided more insights on this possibility; future studies which wanted to fully address the question of Gd excretion should plan to track alloy traces in the litters as well.

Finally, while the EDX results provided semi-quantitative information about relevant elements in the corrosion layer of the implants, none of the techniques that we have used could determine the chemical speciation of the different layers. While one could look at the different ratios between the element concentrations, such as comparing Ca vs P in an attempt to discriminate between different apatites, this would be far from conclusive. Other techniques, such as x-ray absorption spectroscopy (XAS) and in particular x-ray absorption near edge structure (XANES, also known as NEXAFS, i.e. near edge x-ray absorption fine structure) have been already extensively employed to determine the speciation of metals in biomedical tissue [44] and might be able to provide insights on the chemical speciation of Gd and possibly Mg in the corrosion layer. A further advantage of those techniques is that they are commonly available at synchrotron beamlines that also offer XRF, and thus could be effectively combined with elemental mapping within the same beamtime.

As far as neutron tomography is concerned, its intrinsic limit is that it could not provide any information about any other elements except Gd in the corrosion layer, since their signal was overpowered by the Gd one. Nevertheless, the technique was very valuable in detecting small implant fragments in the bone marrow, which could be a promising application for longer healing times, where a larger implant fragmentation can be expected. A combination of x-ray and neutron tomography also seems very promising in the study of other non-Gd based biodegradable alloys, where the absence of Gd could allow more insights on the implant byproducts.

4. Conclusion

This study has successfully employed multimodal imaging techniques to investigate the degradation of Mg-5Gd and Mg-10Gd implants after 12 weeks of healing time in Sprague Dawley rats. The main finding has been that the corrosion appears to involve only the Mg component, while the Gd remains localized at the implant site. This was observed in 2D by means of EDX maps and extended to 3D with a novel application of neutron tomography; XRF analysis of organs also did not reveal any measurable accumulation of Gd, further reinforcing the conclusion that very limited or no removal at all of Gd-alloy happened during degradation.

Small fragments of the implants were detected in the bone marrow and bone close to the implants, but most of the material was still in its original position and from neutron tomography the implant appeared mostly intact.

The 2D elemental analysis of the corrosion layer revealed a progressive substitution of Mg with Ca, P and O. The corrosion layer appeared further subdivided in sub-layers, which could be very well identified in the 3D x-ray µCT scans as well, presenting very different x-ray attenuation coefficients. In particular, an intermediate Ca-rich layer showed very high x-ray attenuation and was also visible in the matching histological sections, but no cellular activity could be detected in it.

A final important result of this work has been exploring the potential of 3D tomographic techniques in the study of implant corrosion, when paired with already well-established 2D techniques. The registration of EDX, histology and x-ray µCT worked reasonably well, allowing to associate different x-ray attenuation values with different elemental compositions. Assuming that the correspondence is consistent across the whole sample, x-ray µCT could provide volumetric information about the remaining non-corroded Mg-rich part; it would also allow to follow the Ca-rich sub-layer and measure its size. Neutron tomography, on the other hand, was crucial in discriminating the Gd distribution in 3D, which would not have been as easily visible with x-ray µCT alone.

Data availability statement

The datasets generated and/or analyzed during the current study are available from the corresponding author upon request.

Funding sources

Funding was provided by the Röntgen-Ångström Cluster in project SynchroLoad (German Federal Ministry of Education and Research grant no. 05K16CGA, Swedish Research Council grant no. 2015-06109). NP and MB were also financially supported by the Swedish Research Council grant number 2014-06054.

Declaration of Competing Interest

The authors declare that they have no known competing financial interests or personal relationships that could have appeared to influence the work reported in this paper.

Acknowledgements

The authors would like to thank Robin Woracek for the guidance in the neutron experiments, Max Viklund for the support

with the EDX scans, Till Dreier for the assistance during the neutron scans and the staff at the P05 beamline at PETRA III DESY for the aid throughout the x-ray scans. This research was supported in part through the Maxwell Computational Resources Operated at Deutsches Elektronen-Synchrotron (DESY), Hamburg, Germany. The experiment at IBL was performed within the beamtimes 11004016, 11004263 and 11005553. We would also like to acknowledge Björn Wiese for the valuable insights regarding the alloy characterization, as well as surgeons David Reinedahl and Pär Johansson for the help during the animal experiments.

Supplementary materials

Supplementary material associated with this article can be found, in the online version, at doi:10.1016/j.actbio.2021.09.047.

References

[1] B.J. Luthringer, F. Feyerabend, R. Willumeit-Romer, Magnesium-based implants: a mini-review, Magnes. Res. 27 (4) (2014) 142–154.
[2] S. Virtanen, Biodegradable Mg and Mg alloys: Corrosion and biocompatibility, Mater. Sci. Eng. B 176 (20) (2011) 1600–1608.
[3] N. Hort, Y. Huang, D. Fechner, M. Stormer, C. Blawert, F. Witte, C. Vogt, H. Drucker, R. Willumeit, K.U. Kainer, F. Feyerabend, Magnesium alloys as implant materials-principles of property design for Mg-RE alloys, Acta Biomater 6 (5) (2010) 1714–1725.
[4] W. Weng, A. Biesiekierski, Y. Li, M. Dargusch, C. Wen, A review of the physiological impact of rare earth elements and their uses in biomedical Mg alloys, Acta Biomater. (2021).
[5] D.R. Broome, M.S. Girguis, P.W. Baron, A.C. Cottrell, I. Kjellin, G.A. Kirk, Gadodiamide-associated nephrogenic systemic fibrosis: why radiologists should be concerned, AJR Am. J. Roentgenol. 188 (2) (2007) 586–592.
[6] M. Ramalho, J. Ramalho, L.M. Burke, R.C. Semelka, Gadolinium retention and toxicity–An update, Adv. Chronic Kidney Dis. 24 (3) (2017) 138–146.
[7] B.A. Biagi, J.J. Enyeart, Gadolinium blocks low- and high-threshold calcium currents in pituitary cells, Am. J. Physiol. 259 (3 Pt 1) (1990) C515–C520.
[8] A. Myrissa, S. Braeuer, E. Martinelli, R. Willumeit-Romer, W. Goessler, A.M. Weinberg, Gadolinium accumulation in organs of Sprague-Dawley(R) rats after implantation of a biodegradable magnesium-gadolinium alloy, Acta Biomater. 48 (2017) 521–529.
[9] T.H. Darrah, J.J. Prutsman-Pfeiffer, R.J. Poreda, M.Ellen Campbell, P.V. Hauschka, R.E. Hannigan, Incorporation of excess gadolinium into human bone from medical contrast agents, Metallomics 1 (6) (2009) 479–488.
[10] B. Zeller-Plumhoff, C. Malich, D. Kruger, G. Campbell, B. Wiese, S. Galli, A. Wennerberg, R. Willumeit-Romer, D.C.F. Wieland, Analysis of the bone ultrastructure around biodegradable Mg-xGd implants using small angle X-ray scattering and X-ray diffraction, Acta Biomater. 101 (2020) 637–645.
[11] T.A. Grunewald, H. Rennhofer, B. Hesse, M. Burghammer, S.E. Stanzl-Tschegg, M. Cotte, J.F. Loffler, A.M. Weinberg, H.C. Lichtenegger, Magnesium from bioresorbable implants: distribution and impact on the nano- and mineral structure of bone, Biomaterials 76 (2016) 250–260.
[12] R. Delfino, M. Biasotto, R. Candido, M. Altissimo, M. Stebel, M. Salome, J.T. van Elteren, K. Vogel Mikus, C. Zennaro, M. Sala, R. Addobbati, G. Tromba, L. Pascolo, Gadolinium tissue deposition in the periodontal ligament of mice with reduced renal function exposed to Gd-based contrast agents, Toxicol. Lett. 301 (2019) 157–167.
[13] A. Turyanskaya, M. Rauwolf, T.A. Grünewald, M. Meischel, S. Stanzl-Tschegg, J.F. Löffler, P. Wobrauschek, A.M. Weinberg, H.C. Lichtenegger, C. Streli, μXRF elemental mapping of bioresorbable magnesium-based implants in bone, Materials 9 (10) (2016).
[14] C. Streli, M. Rauwolf, A. Turyanskaya, D. Ingerle, P. Wobrauschek, Elemental imaging of trace elements in bone samples using micro and nano-X-ray fluorescence spectrometry, Appl. Radiat. Isotopes 149 (2019) 200–205.
[15] M. Esmaily, J.E. Svensson, S. Fajardo, N. Birbilis, G.S. Frankel, S. Virtanen, R. Arrabal, S. Thomas, L.G. Johansson, Fundamentals and advances in magnesium alloy corrosion, Prog. Mater. Sci. 89 (2017) 92–193.
[16] S. Sanyal, P. Marckmann, S. Scherer, J.L. Abraham, Multiorgan gadolinium (Gd) deposition and fibrosis in a patient with nephrogenic systemic fibrosis–an autopsy-based review, Nephrol. Dial. Transpl. 26 (11) (2011) 3616–3626.
[17] N. Kardjilov, I. Manke, R. Woracek, A. Hilger, J. Banhart, Advances in neutron imaging, Mater. Today 21 (6) (2018) 652–672.
[18] M. Jacot-Guillarmod, K. Schmidt-Ott, D. Mannes, A. Kaestner, E. Lehmann, C. Gervais, Multi-modal tomography to assess dechlorination treatments of iron-based archaeological artifacts, Herit. Sci. 7 (1) (2019) 29.
[19] J. Moosmann, B. Zeller-Plumhoff, D.C.F. Wieland, S. Galli, D. Krüger, T. Dose, H. Burmester, F. Wilde, M. Bech, N. Peruzzi, B. Wiese, A. Hipp, F. Beckmann, J. Hammel, R. Willumeit-Römer, doi:10.1117/12.2275121.
[20] D. Krüger, B. Zeller-Plumhoff, B. Wiese, S. Yi, M. Zuber, F. Wieland, J. Moosmann, R. Willumeit-Römer, Assessing the microstructure and in vitro degradation behaviour of Mg-xGd screw implants using μCT, J. Magnes. Alloy. (2021) (In press), doi:10.1016/j.jma.2021.07.029.
[21] F. Feyerabend, M. Johannisson, Z. Liu, R. Willumeit-Römer, Influence of various sterilization methods on hardness, grain size and corrosion rate of a Mg6Ag-alloy, BioNanoMaterials 16 (1) (2015) 51–58.
[22] J. Moosmann, A. Ershov, V. Weinhardt, T. Baumbach, M.S. Prasad, C. LaBonne, X. Xiao, J. Kashef, R. Hofmann, Time-lapse X-ray phase-contrast microtomography for in vivo imaging and analysis of morphogenesis, Nat. Protoc. 9 (2) (2014) 294–304.
[23] W. van Aarle, W.J. Palenstijn, J. De Beenhouwer, T. Altantzis, S. Bals, K.J. Batenburg, J. Sijbers, The ASTRA toolbox: a platform for advanced algorithm development in electron tomography, Ultramicroscopy 157 (2015) 35–47.
[24] W. van Aarle, W.J. Palenstijn, J. Cant, E. Janssens, F. Bleichrodt, A. Dabravolski, J. De Beenhouwer, K.J. Batenburg, J. Sijbers, Fast and flexible X-ray tomography using the ASTRA toolbox, Opt. Express 24 (22) (2016) 25129–25147.
[25] W.J. Palenstijn, K.J. Batenburg, J. Sijbers, Performance improvements for iterative electron tomography reconstruction using graphics processing units (GPUs), J. Struct. Biol. 176 (2) (2011) 250–253.
[26] N. Kardjilov, A. Hilger, I. Manke, CONRAD-2: Cold neutron tomography and radiography at BER II (V7), J. Large Scale Res. Facil. JLSRF 2 (2016).
[27] N. Kardjilov, A. Hilger, I. Manke, R. Woracek, J. Banhart, CONRAD-2: the new neutron imaging instrument at the Helmholtz-Zentrum Berlin, J. Appl. Crystallogr. 49 (1) (2016) 195–202.
[28] S.H. Williams, A. Hilger, N. Kardjilov, I. Manke, M. Strobl, P.A. Douissard, T. Martin, H. Riesemeier, J. Banhart, Detection system for microimaging with neutrons, J. Instrum. 7 (02) (2012) P02014–P02014.
[29] B. Munch, P. Trtik, F. Marone, M. Stampanoni, Stripe and ring artifact removal with combined wavelet–Fourier filtering, Opt. Express 17 (10) (2009) 8567–8591.
[30] A.P. Kaestner, MuhRec—A new tomography reconstructor, Nucl. Instrum. Methods Phys. Res. Section A: Accel. Spectrom. Detect. Assoc. Equip. 651 (1) (2011) 156–160.
[31] K. Donath, M. Rohrer, Bone Sectioning Using the Exakt System, in: Y.H. An, K.L. Martin (Eds.), Handbook of Histology Methods for Bone and Cartilage, Humana Press, Totowa, NJ, 2003, pp. 243–252.
[32] H. Helmholz, B.J.C. Luthringer-Feyerabend, R. Willumeit-Römer, Elemental mapping of biodegradable magnesium-based implants in bone and soft tissue by means of μ X-ray fluorescence analysis, J. Anal. At. Spectrom. 34 (2) (2019) 356–365.
[33] J. Moosmann, D.C.F. Wieland, B. Zeller-Plumhoff, S. Galli, D. Krüger, A. Ershov, S. Lautner, J. Sartori, M. Dean, S. Köhring, H. Burmester, T. Dose, N. Peruzzi, A. Wennerberg, R. Willumeit-Römer, F. Wilde, P. Heuser, J. Hammel, F. Beckmann, A Load Frame For In Situ Tomography at PETRA III, SPIE, 2019.
[34] N. Angrisani, J. Reifenrath, F. Zimmermann, R. Eifler, A. Meyer-Lindenberg, K. Vano-Herrera, C. Vogt, Biocompatibility and degradation of LAE442-based magnesium alloys after implantation of up to 3.5years in a rabbit model, Acta Biomater. 44 (2016) 355–365.
[35] B. Zeller-Plumhoff, H. Helmholz, F. Feyerabend, T. Dose, F. Wilde, A. Hipp, F. Beckmann, R. Willumeit-Römer, J.U. Hammel, Quantitative characterization of degradation processes in situ by means of a bioreactor coupled flow chamber under physiological conditions using time-lapse SRμCT, Mater.Corros. 69 (3) (2018) 298–306.
[36] B. Zeller-Plumhoff, M. Gile, M. Priebe, H. Slominska, B. Boll, B. Wiese, T. Würger, R. Willumeit-Römer, R.H. Meißner, Exploring key ionic interactions for magnesium degradation in simulated body fluid–A data-driven approach, Corros. Sci. 182 (2021).
[37] N.Ahmad Agha, R. Willumeit-Romer, D. Laipple, B. Luthringer, F. Feyerabend, The degradation interface of magnesium based alloys in direct contact with human primary osteoblast cells, PLoS One 11 (6) (2016) e0157874.
[38] I. Marco, A. Myrissa, E. Martinelli, F. Feyerabend, R. Willumeit-Romer, A.M. Weinberg, O. Van der Biest, *In vivo* and *in vitro* degradation comparison of pure Mg, Mg-10Gd and Mg-2Ag: a short term study, Eur. Cell Mater. 33 (2017) 90–104.
[39] H. Rauch, W. Waschkowski, Neutron scattering lengths in, in: A.J. Dianoux, G. Lander (Eds.), ILL Neutron Data Booklet Eds., Old City Publishing, Philadelphia, PA, 2003 1.1–1 to 1.1–17.
[40] V.F. Sears, Scattering lengths for neutrons, in: E. Prince (Ed.), International Tables for Crystallography Ed., Kluwer Academic Publishers, 2006.
[41] M. Hascke, Laboratory Micro-X-Ray Fluorescence Spectroscopy: Instrumentation and Applications, Springer.
[42] H. Helmholz, O. Will, T. Penate-Medina, J. Humbert, T. Damm, B. Luthringer-Feyerabend, R. Willumeit-Romer, C.C. Gluer, O. Penate-Medina, Tissue responses after implantation of biodegradable Mg alloys evaluated by multimodality 3D micro-bioimaging in vivo, J. Biomed. Mater. Res. A (2021).
[43] J. Miyawaki, S. Matsumura, R. Yuge, T. Murakami, S. Sato, A. Tomida, T. Tsuruo, T. Ichihashi, T. Fujinami, H. Irie, K. Tsuchida, S. Iijima, K. Shiba, M. Yudasaka, Biodistribution and ultrastructural localization of single-walled carbon nanohorns determined in vivo with embedded Gd2O3 labels, ACS Nano 3 (6) (2009) 1399–1406.
[44] F. Porcaro, S. Roudeau, A. Carmona, R. Ortega, Advances in element speciation analysis of biomedical samples using synchrotron-based techniques, TrAC Trends Anal. Chemistry 104 (2018) 22–41.